Sedsel Fretheim Thomassen

InAs/(Al)GaAs quantum dots for intermediate band solar cells

NTNU
Innovation and Creativity

Abstract

Intermediate band solar cells (IBSCs) have a theoretical conversion efficiency limit of 63.2%, compared to 40.7% for a single junction solar cell. The enhanced efficiency limit is due to an intermediate energy level positioned inside the semiconductor bandgap, which allows absorption of both low and high energy photons without severe energy loss of solar cell voltage. The intermediate band can be formed by introducing quantum dots (QDs) into the semiconductor. Self-assembled QDs can be grown by molecular beam epitaxy (MBE).

A handful of groups world wide attempt to fabricate InAs/GaAs QD-IBSCs, but no large efficiency improvements has yet been reported. There are several reasons for the lack of success. One of them is the choice of the InAs/GaAs material system, another is defect formation during QD growth. With optimized growth conditions, formation of defect free QD materials is possible. The challenge is to obtain defect free QD materials with the desired properties for QD-IBSCs. The main topic of this thesis has therefore been to optimize the growth conditions used during MBE growth in order to achieve a high density of small QDs with a narrow size distribution. At the same time it is important to avoid formation of defects deteriorating the optical material quality, and the performance of the solar cells.

A systematic study of the influence of MBE growth parameters on the QD densities, size distributions and optical performance was performed. The substrate temperature during QD growth, the InAs growth rate, the In:As$_2$ flux ratio, and the InAs thickness were varied systematically. The InAs QDs were grown either on GaAs or Al$_{0.35}$Ga$_{0.65}$As. For growth on GaAs, the deposition method for InAs was also studied. Large ensembles of up to 12700 QDs for each sample where characterized by scanning electron microscopy (SEM), and atomic force microscopy (AFM). The extremely high QD densities ($> 10^{11}$ cm^{-2}) and the small QDs sizes (down to sub-nm heights, and < 10 nm in diameter) made the imaging extremely challenging. Most of the samples showed bimodal growth, and a complete explanation

of the formation process is given in the thesis. Photoluminescence (PL) characterization revealed a close connection between the density of large QDs (ρ_L) and the PL intensity. The optical material quality is reduced for QD densities above a certain limit.

Three batches of QD-IBSCs were made and characterized as part of this thesis. We found a slightly enhanced short current density due to the presence of the QD layers. However, the main enhancement is most likely due to the two-dimensional wetting layer positioned below the QDs as it seems to be independent of QD density. The first batch of solar cells showed degradation of the n-base due to the thermal cycling when the QD stack was grown. In the second batch of QD-IBSCs, we removed the WL between the InAs QDs by capping the QDS with AlAs before the GaAs spacers were deposited. In the third batch of solar cells, we successfully fabricated the first InAs/AlGaAs QD-IBSC in the world. The EQE spectra showed that the IB is shifted deeper into the bandgap, as desired.

The thesis hopefully sheds light on important aspects on how to, and how not to, fabricate Qd-IBSCs in order to achieve enhanced conversion efficiencies in the future.

Preface

The work in this thesis was carried out at the Department of Physics at the Norwegian University of Science and Technology (NTNU) from September 2005 to June 2012. The project I am part of is a collaboration between the Solar cell physics group at the Department of Physics and the Electronic devices and materials group at the Department of Electronics and Telecommunications.

One of the more surprising findings during my work has been that, despite the 5000 reported papers on InAs/GaAs quantum dots (QDs), the growth mechanisms and formation of the QDs are still not fully understood. To complicate things even more, every MBE machine is different and studies of the influence of the MBE growth parameters should be performed in every lab. These studies, that were supposed to be pre-studies, turned out to be the main topic of my thesis as we found interesting features in almost all grown samples. The pre-studies were expanded to get a deeper understanding of each growth parameter. Today, around 100 samples later, I still find new and interesting information when looking at SEM and AFM images or at a PL spectrum. However, it is time for closure and time to present the overwhelming amount of results.

Early in the project period, I went to Chalmers University of Technology to learn how to grow QDs and to Linköping University to study the optical properties of the Chalmers-grown QDs. However, all the QD samples in the studies included in this thesis are grown in the MBE lab at Department of Electronics and Telecommunications at NTNU. All SEM characterization was performed at Department of Materials Technology at NTNU, while AFM studies were performed partly at Department of Physics, Department of Electronics and Telecommunications and at SINTEF. TEM characterization of the QD materials are performed by Per-Erik Vullum at Department of Physics and PL characterization by Maryam Gholami Mayani during a stay at Linköping University.

Acknowledgements

A number of people have been of great value to me, both professionally and personally. First of all I have to thank my supervisor Turid Worren Reenaas for believing in me from the first moment. Turid is always humorous, energetic, full of ideas, devoted and helpful. I also want to thank Turid for a great friendship. My co-supervisor, Bjørn-Ove Fimland, is appreciated for his patience, calmness, knowledge and sense of humor. I also want to thank him for believing in me through the though spring of 2010. Both supervisors have given me the opportunity to work independently, forming own ideas and plans. I am deeply thankful for the the opportunity and hope I have used it well.

I especially want to thank Shumin Wang and Mahdad Sadeghi at Chalmers University of Technology. They were two important corner stones early in my project with their openness, willingness to share knowledge and enthusiasm. Mahdad's good mood during a long day in the MBE lab has been an inspiration to me during hard periods of lab work at NTNU. Per-Olof Holtz and his ph.d students at Linköping University deserves acknowledgement for help during PL characterization of a large portion of my samples. I thank Per-Erik Vullum for his TEM work on several samples, giving us important information of several aspects of the QD growth. Estela Hernández and Irene Artacho Huertas deserves acknowledge for their intense work with metalization, EQE and IV characterization of a large number of QD-IBSCs. I am grateful both to them and to Antonio Martí Vega for their openness and cooperation. Tor Arild Nilsen and Yingda Yu deserves acknowledge for always being helpful and sharing their good mood during search seeks for tiny QDs by SEM.

It was a pleasure to share office with Rune the first years, which included discussion around topics spanning from solar cell physics to re-decoration. He should be acknowledged for bearing through periods where no equipment was working and times with a large amount baby talk due to series pregnancies in the group. When Rune finished his ph.d, Maryam became my new room mate. Maryam has been a great support during long lab hours and has become a good friend. I am also thankful for her effort on PL characterization of all the QD samples. I want to thank all my co-growers at the MBE-lab, Magnus, Tron Arne, Dheeraj and Saroj for making a nice atmosphere inside the otherwise slightly depressive laboratory and for loading/de-loading samples in the periods when I was pregnant. Especially Tron deserves acknowledge for always helping, and never resigning, when the MBE is troublesome. I also want to thank Geir for his patience with

Contents

Paper I
InAs/GaAs quantum dot density variation across a quarter wafer when grown with substrate rotation

Paper II
Correlation between size distribution and optical quality of large ensembles of high-density InAs/GaAs quantum dots

Paper III
On the nucleation and mass transport during formation of bimodal InAs/GaAs quantum dots

Paper IV
On the formation of large-sized InAs/GaAs quantum dots

Paper V
Removal of the wetting layer in InAs/GaAs quantum dot materials

Paper VI
Systematic study of the influence of growth parameters on InAs/Al$_{0.35}$Ga$_{0.65}$As quantum dot and wetting layer properties

Paper VII
Base degradation of InAs/GaAs quantum dot intermediate band solar cells

Paper VIII

Enhanced open circuit voltage in an InAs/GaAs quantum dot intermediate band solar cell due to wetting layer removal

Paper IX
InAs/Al$_{0.35}$Ga$_{0.65}$As quantum dot intermediate band solar cells grown by MBE

Chapter 1

Introduction

Today's society is completely dependent on fossil energy, in the form of coal, oil and gas, and nuclear energy. Although new fields of coal, oil, and gas are still found from time to time, the world's reservoirs of fossil fuel will empty sooner or later. The use of fossil fuels has a negative impact on the environment and is with a large certainty responsible for the global warming. Alternative energy sources must therefore be found. The available energy sources are illustrated in Figure 1.1. Actually, all sources in the figure, except geothermal and nuclear energy, originates directly or indirectly from solar energy [1].
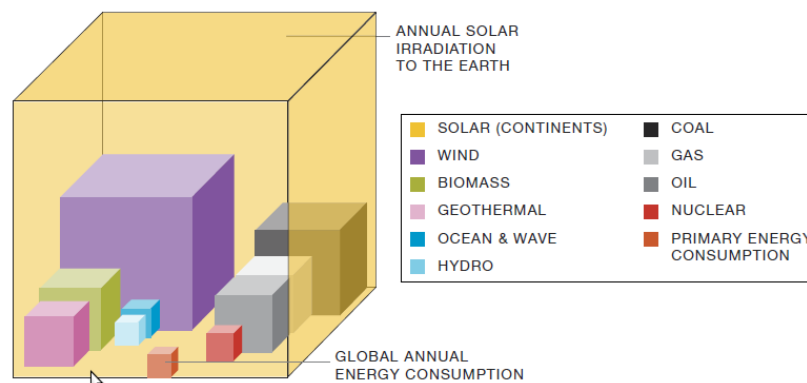

Figure 1.1: Total annual solar irradiation (orange cube) compared to established energy resources. The cubes representing coal, gas and oil illustrate the amount of energy that can be converted from the known reserves. The renewable energy sources are shown as the yearly potential. Taken from [2].

A combination of several types of renewable energy sources must replace

the non-renewable. One of the promising technologies is solar cells, also known as photovoltaics. Using today's solar cell technology, each square meter on Earth can on average generate 1700 kWh every year [2]. If the whole Earth was covered in such solar cells, the total annual generation of energy would be 10.000 times larger than the existing global annual energy need. The reader should keep in mind that solar cells is only one technology for exploiting solar energy. Several possibilities also exist in terms of solar thermal energy [3]: By passive heating, houses can be heated solely by the sun, often including solar hot water systems where water is heated by a solar collector. In solar electricity thermal power, sun light is used to heat the water in steam generators to produce electricity.

The photovoltaic (PV) industry has experienced a strong positive development during the last years, as shown in Figure 1.2. The European Photovoltaic Industry Association [4] and Greenpeace [5] has jointly established global solar scenarios for the PV market six times since 2001. Every year, the actual global PV market has grown faster than their predictions [2]. As an example, in the first report from 2001, they predicted a total installation of 1700 MW in 2008, while the real result was 3.6 times larger. However, only 0.2 % of the World's demand for electricity was met by PV energy in 2010 and the potential for further growth of the solar industry is large.
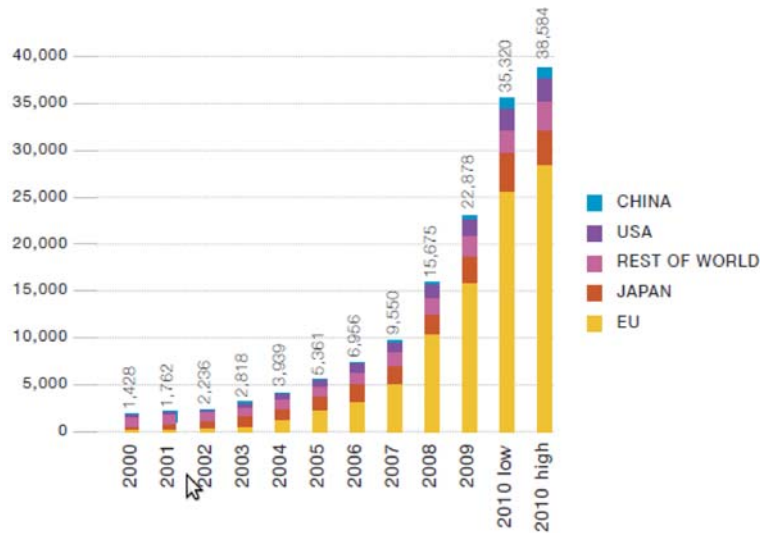

Figure 1.2: Capacity of installed solar cells between year 2000 and 2010. 53 % of the PV installations in Europe is in Germany. Taken from [2].

The crystalline silicon (c-Si) solar cell is the most common solar cell having 80 % of the total market. c-Si cells convert 14-22 % of the solar irradiation impinging the cell to electricity. The only commercial PV technology with higher conversion efficiencies are III-V multi junction solar cells, with conversion efficiencies above 30%. The current conversion efficiency record at 43.5% was reported in April last year and was achieved with a GaInP/GaAs/GaInNAs triple junction solar cell [6, 7].

Multi junction and c-Si solar cells represent two different generations solar cells. c-Si solar cells belong to the first generation of solar cells. Fabrication of the these cells is expensive and the conversion efficiencies are modest, resulting in expensive electricity, see Figure 1.3. Second generation solar cells includes solar cells with low conversion efficiency and low manufacture cost. The price per Watt is lower than for the first generation solar cells. The solar cell conversion efficiency of first and second generation solar cells is limited by the Shockley-Queisser limit at 40.7% [8].

Multi junction solar cells belong to the third generation. The long term aim for this generation is to achieve high conversion efficiencies at low production cost, resulting in a very low price per Watt. Within each generation, several technologies exist, which currently are studied by research groups world wide. The topic of this thesis, quantum dot intermediate band solar cells, belong to the third generation solar cells.
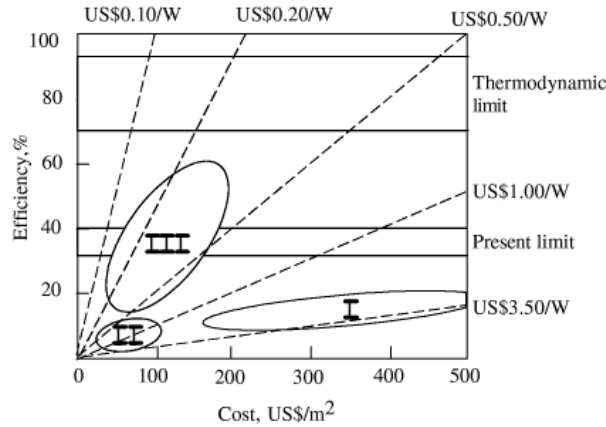

Figure 1.3: The three solar cell generations (I, II and III) are defined from their efficiency and cost. Research on third generation solar cells aim to reduce the total price on the produced electricity by increasing the solar cell efficiency above the Shockley-Queisser limit without raising the fabrication cost too much. Taken from [9].

This thesis is a tiny piece in the puzzle, which in the end hopefully turns out to be a breakthrough for the solar cell development. The results in this thesis give insight in how to, and how not to, improve the quality of quantum dot (QD) materials for intermediate band solar cells (IBSCs). This insight is also useful for other research fields, as e.g. quantum dot lasers and quantum dot detectors, which also benefit from the unique properties of the quantum dots. In addition, we aim to contribute to the understanding of the formation of self-organized quantum dots.

This thesis is the first step for our research group toward realization a QD-IBSC with a high conversion efficiency. Part I therefore contains an introduction to solar cells. However, the main focus has been to understand and control the QD growth to achieve QD ensembles with appropriate properties for reaching increased conversion efficiencies when introduced in solar cells.

The thesis is divided into two parts. Part I starts with a motivation of why we study third generation solar cells (Chapter 1 and 2) and a presentation of different types of third generation solar cells aiming for high efficiencies (Chapter 3). The different characterization techniques are described in Chapter 4 along with a presentation of fabrication of QDs with molecular beam epitaxy (MBE). Only a short description of the QD formation is given as this topic is thoroughly discussed in Papers I-VI. Chapter 4 would normally include a literature review of previous work. Such a list is practically impossible to present as around 5000 studies are reported on the InAs/GaAs quantum dot material system. Instead, the status, challenges and proposed solutions of InAs/(Al)GaAs quantum dot intermediate band solar cells are presented, in Chapter 5, together with our contributions on the topic. A summary of the papers is given in Chapter 6.

Part II includes my scientific work presented in the form of papers that already have been published (Paper I), or as manuscripts (II-IX).

My contribution to the included papers are design and MBE growth of almost all QD samples and solar cell samples, all SEM characterization, about 50 % of the AFM characterization, and data analysis of results from PL, QE and IV characterization. The choice of research direction, samples and sample design were determined together with my supervisors.

Chapter 2

Conventional solar cells

In this chapter, the physics of the conventional solar cell including its main loss mechanisms will be presented. Third generation solar cells aim to reduce these energy losses. The main types of third generation solar cells are presented, but a detailed description is only given for the intermediate band solar cell. As the work carried out is experimental, only the solar cell physics needed to understand the performed solar cell characterization is presented.

2.1 Solar cell physics

A conventional solar cell essentially consist of a semiconductor pn-junction positioned between two metal contacts [10–12]. The p-side is a p-doped semiconductor, where the Fermi level lies near the valence band (VB) due to an excess of positive charge carriers (holes). The n-side is a n-doped semiconductor with an excess of negative carriers (electrons). Here, the Fermi level lies near the conduction band (CB). The volume near the junction is depleted of free carriers as the free positive carriers close to the p-side diffuse to the n-side, and opposite for the free negative carriers, until the two Fermi levels are aligned. An electric field is formed by the space charges due to the ionized dopants, see Figure 2.1a), inhibiting further carrier diffusion. The potential difference between the p and n side (V_{bi}) is called the 'built-in' potential.

   Under illumination by photons with energy higher than the bandgap, electrons from VB can be excited to the CB. Electrons situated on the p-side can diffuse towards the junction and be swept to the n side by the electric field. If they are not immediately extracted to the external circuit, the number of majority carriers on each side, i.e. holes on the p-side and
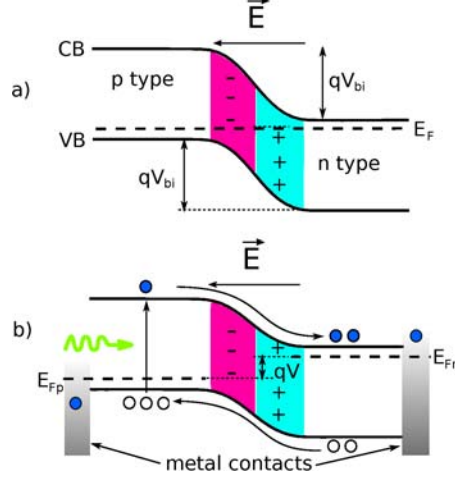
Figure 2.1: pn junction a) in equilibrium and b) under illumination.

electrons on the n-side, will increase compared to the situation without illumination. Then the electrons on the n-side will have higher potential energy than the electrons on the p-side. This is illustrated by the Fermi level splitting in Figure 2.1b). The height of the potential barrier between the n and p side is then reduced.

The net current density in the solar cell is

$$I(V) = I_{sc} - I_{dark}(V) = I_{sc} - I_0(e^{\frac{qV}{k_B T}} - 1), \qquad (2.1)$$

where I_{sc} is the short circuit current, I_0 is the saturation reverse current, q is the elementary charge, V is the voltage over the cell, k_B is Boltzmanns constant and T the cell temperature. When no load is present, i.e. the terminals are short circuited, $I = I_{sc}$. When the terminals are disconnected, $I = 0$ and $V = V_{oc}$, the open circuit voltage. The solar cell will be operated in the regime $[I, V] = [(0, I_{sc}), (0, V_{oc})]$. The generated power is given by

$$P = IV, \qquad (2.2)$$

which reaches a maximum at $P_{max} = I_m V_m$, as illustrated in Figure 2.2.
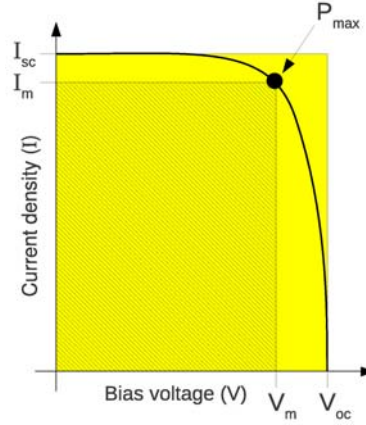
Figure 2.2: Current-voltage characteristics of an ideal solar cell. The maximum power density is reached when $I = I_m$ and $V = V_m$. The fill factor is the area of the shaded area divided by the area of the yellow area.

2.2 Loss mechanisms

There are mainly five energy conversion loss processes in a conventional solar cell [9]:

1. Low energy photons are not absorbed

2. Thermalization loss

3. Recombination loss

4. Junction loss

5. Contact loss

The loss mechanisms are illustrated in Figure 2.3 and further described below:

1. The semiconductor material is transparent for photons with energy lower than the bandgap. The bandgap of a conventional Si solar cell is 1.1 eV, which corresponds to 1128 nm. All photons with higher wavelengths are transmitted through the solar cell, and can be accounted for as energy loss, as illustrated in Figure 2.4. A larger amount of the solar spectrum is absorbed in a material with lower bandgap, but the cell voltage is then reduced, as illustrated in Figure 2.1. As the solar cell power is $P = IV$, both the current (I) and the voltage (V) must be optimized.
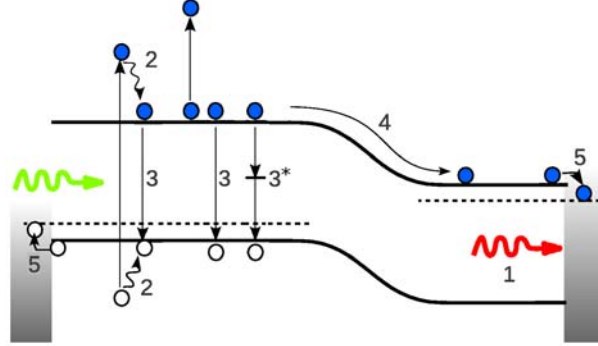
Figure 2.3: The main energy loss mechanisms in a solar cell: 1. Low energy photons that are not absorbed, 2. Thermalisation loss, 3. non-avoidable (radiative and Auger) recombination loss, 3*. avoidable (defect/impurity related) recombination loss, 4. junction loss and 5. contact loss.
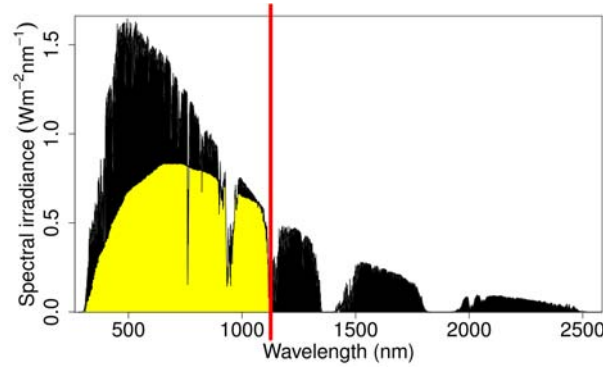
Figure 2.4: The AM 1.5 solar spectrum: The solar spectrum at sea level after traveling through 1.5 times the atmosphere thickness. The red line shows the wavelength corresponding to the bandgap energy of silicon. In a Si solar cell, the photons with lower energy (longer wavelengths) are transmitted through the cell. High energy photons loose the excess energy due to thermalization. The yellow area illustrates the exploited part of the solar spectrum.

2. If a photon with energy (E_{ph}) higher than the bandgap (E_g) is absorbed, an electron is excited across the bandgap to a state with high kinetic energy [10]. The electron will rapidly thermalize due to repeated collisions with atoms/ions and electrons until the electron reaches the conduction band edge. The excess energy ($E_{ph} - E_g$) is not exploited in the solar cell and is lost. This loss can reduced using a high band gap semiconductor.

However, then the number of absorbed photons would be low, and then also the current.

3. Recombination is a joint denotation of several mechanisms which result in the loss of electron-hole pairs and is divided into two groups: non-avoidable (3) and avoidable (3*) [10]. Two mechanisms are not avoidable: Radiative and Auger recombination. Radiative recombination, or spontaneous emission, occurs when an electron in the CB recombines with a hole in the VB and simultaneously emits a photon. In Auger recombination, two electrons in the CB interact and cause one of the electrons to recombine with a hole in VB. The other electron gains an amount of kinetic energy equal to the energy released in the recombination of the electron and the hole. The main avoidable loss mechanism is called Shockley-Read-Hall recombination and involve recombination via a localized deep energy state formed by defects or impurities in the solar cell material. All three mechanisms result in removal of electrons or holes.

4. The electron looses energy when it drifts across the junction from the p side to the n side, and opposite for the holes drifting in the opposite direction. A larger potential barrier results in a larger energy loss.

5. The electrons on the n side will be collected by the contact. If the Fermi level of the contact material is lower than the electron quasi Fermi level (E_{Fn}), the excess energy will be lost. A similar loss mechanisms will occur for the holes collected by the contact on the n side.

In 1960 Shockley and Queisser reported the well known detailed balance limit of solar cell efficiency of 40.7%, assuming an ideal solar cell illuminated with fully concentrated black body radiation (6000 K), absorption of all incoming photons with energy larger than the bandgap, and including only radiative recombination and thermalization losses [8]. For unconcentrated light, the conversion limit is 30.5 % [13]. Up to date, efficiencies of 25% and 28% are achieved for Si and GaAs single junction solar cells, respectively, under unconcentrated light [7].

Chapter 3

Third generation solar cells

Third generation solar cells have efficiency limits that are above the limit for the 1st and 2nd generation cells (the Shockley-Queisser limit). If high conversion efficiencies are achieved without increasing cost in material fabrication too much, the cost of electricity will be low compared to the first generations of solar cells (single junction cells). The main losses in a single junction solar cell are loss of photons with energy lower than the material bandgap and thermalization loss for charge carriers exited by high energy photons, as described in Section 2.2. The third generation cells are designed so that these losses are reduced.

3.1 Above the Shockley-Queisser limit

There are two routes of exceeding the Shockley-Queisser limit. In route I the incoming solar spectrum is modified to be better exploited in a single junction solar cell, while the solar cells are adjusted to better utilize the solar spectrum in route II.

Route I involves light conversion layers [14]. A down-conversion layer converts one high energy photon to two (or more) photons with lower energy, while an up-conversion layer converts two (or more) low energy photons into one photon with higher energy. The converted photons must of course have energies larger than the bandgap of the solar cell.

Several novel ideas are proposed within route II. These ideas are based on

- collection of hot carriers before they thermalize,

- impact ionization, in addition to photogeneration, and

- introducing more than one bandgap

In a hot carrier solar cell, the cell aim to preserve the energy of the (hot) carriers excited high into the energy bands by high energy photons. In an impact ionization cell, collisions between carriers with energy more than twice the bandgap energy can create a second electron-hole pair in a reverse Auger recombination process. Multiple bandgaps in a cell can be achieved in two ways: Either by making several different single junction cells with different bandgap, each exploiting a part of the solar spectrum, or by making a single cell with a material having several bandgaps. The first solution result in a tandem/multijunction cell, and the second in an intermediate band cell. A more detailed description of the third generation solar cell concept are given in [9].

In the intermediate band solar cell (IBSC), the bandgap contains at least one additional energy band, the intermediate energy band (IB) [15], as illustrated in Figure 3.1. As before, the bandgap between VB and CB is called E_g. The IB effectively introduces two additional bandgaps smaller than E_g. The smallest bandgap is called E_L and the medium bandgap E_H. In an IBSC there are two routes to create photogenerated carriers: Electrons in VB can be excited directly from the VB to the CB by photons with energy $E_{ph} > E_g$. In addition, electrons in the VB can be excited to the IB by photons with $E_{ph} > E_H$, and electrons in the IB can be excited to the CB by photons with $E_{ph} > E_L$. The IB should be partially filled with electrons so all transitions are possible. If the IB is (always) empty, only the transition from VB to IB will take place, while only the transition from the IB to the CB will be possible if the IB is always full.
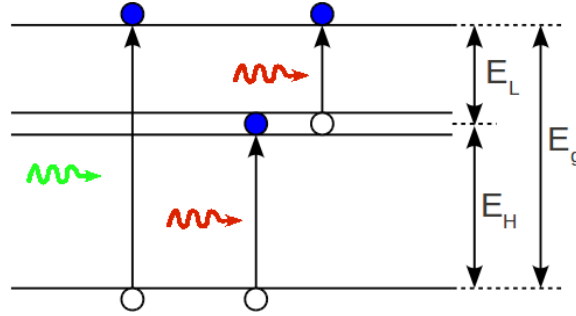

Figure 3.1: Schematic energy diagram of the intermediate band solar cell.

The voltage of the solar cell is given by the difference between the quasi-Fermi levels of the majority carriers in the emitters like in a normal single

junction solar cell. If the IB is isolated from the external contacts, a high voltage (limited by E_g and not E_H or E_L) can be maintained simultaneously as current enhancement is possible trough absorption of sub-bandgap photons [16].

It might seem like a bad idea to introduce an extra energy band in the bandgap, as energy states within the bandgap is normally accompanied by non-radiative Shockley Read Hall recombination. However, if the electronic states participating in forming the IB come from a periodic potential, the electron wavefunction is de-localized and radiative recombination via the IB will dominate over the Shockley Read Hall recombination [16]. If, in addition, the carrier relaxation within the bands is faster than the carrier recombination between bands, each energy band contain its own quasi-Fermi level [17].

For unconcetrated light, the maximum IBSC efficiency is 49.4 % for $E_H = 1.5$ eV and $E_L = 0.95$ eV [18]. As the width of IB is assumed to be zero, the total semiconductor bandgap is $E_g = E_H + E_L = 2.45$ eV. For fully concentrated light, the maximum efficiency for an IBSC is 63.2 % for bandgaps $E_H = 1.24$ eV, $E_L = 0.71$ eV and $E_g = 1.95$ eV [19]. There are several routes to form the intermediate band. So far, most attention has been given to IB formation using arrays of quantum dots.

3.2 The quantum dot intermediate band solar cell

In a bulk crystal material, the free charge carriers (electrons in the CB and holes in the VB) are free to move in three dimensions (3D). The density of states is then a continuous function of energy, see Figure 3.2a), i.e. charge carriers with high kinetic energy will quickly thermalize due to collisions with the lattice since there are always a state to relax to. A nm thin quantum well (QW) is a quasi-2D system. In the QW, made of a thin layer of a low bandgap semiconductor embedded in a large bandgap material, the carriers are confined in one dimension, but free to move in the other two, see Figure 3.2b). The depth of the confining potential well for electrons in the CB equals the conduction band offset between the two semiconductor materials. The density of the confined states is a step function of energy. In a nm sized quantum dot (QD), made of a low bandgap nanocrystal embedded in a large bandgap material, the carriers are confined in all three dimensions and we have a quasi 0D system, see Figure 3.2c). Now, the density of states function consist of delta functions in energy and thus resembles the density of states of an atom. QDs are therefore often called artificial atoms.

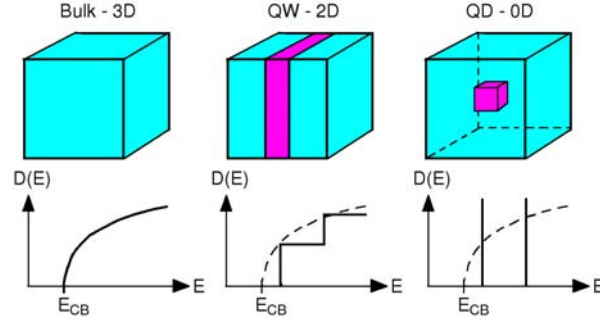The position of the quantized energy levels in the QD is dependent on the

Figure 3.2: Structure and density function states (DE) of structures with different dimensionality. Inspired by [20].

depth of the confining potential and the size of the QD. The first quantized energy level increases with increasing well depth and with decreasing QD size. It is important to mention that for self-assembled InAs/(Al)GaAs QDs, the aspect ratio (height divided by diameter) is < 1 with heights typically in the range 2-20 nm. Changes in QD height therefore has a much stronger influence on the QD energy levels than the QD diameter.

If the QD separation is small, the wavefunctions of carrier in neighboring QDs can overlap. Then the energy levels can couple and form energy minibands, see Figure 3.3c). If the QDs are equally sized, equally separated and have identical composition and strain, the width of the energy level will be at its minimum, but still be > 0. However, in practical QD systems made of self-organized QDs, see Chapter 4, both size and spacing, and possibly also composition and local strain, varies. The result is an inhomogeneous broadening of the band due to different energy levels of the QDs.
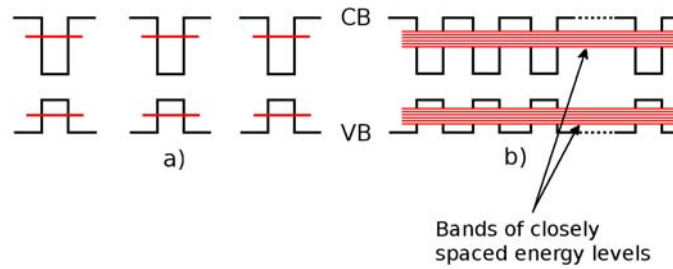
Figure 3.3: Schematic energy band diagram of QD structures where the energy levels are a) localized and b) de-localized.

The quantum dots are normally placed inside the solar cell's pn junction to achieve effective splitting of the photogenerated electron-hole pairs. The optimum bandgaps for reaching the maximum efficiency were listed in Chapter 3. By tuning the growth parameters and materials used for QD growth, the energy levels can be tuned to obtain (effective) bandgaps E_H and E_L that matches the ideal values. A more detailed description of the quantum dot intermediate band solar cell (QD-IBSC) will be given in Chapter 5. Despite the extensive studies of the QD-IBSC, e.g. [21–34], no huge improvement in efficiency has yet been reported.

Chapter 4

Experimental methods

In this chapter, the experimental techniques used are described. All samples included in this thesis are grown by molecular beam epitaxy (MBE) and characterized by a number of characterization techniques. The experimental techniques used by me are described in detail (MBE, RHEED, SEM and AFM), while the other (TEM, PL, IV, and EQE) are only briefly presented and included for completeness.

4.1 Molecular beam epitaxy

In this section the MBE machine and material growth processes during formation of self-assembled QDs are presented.

4.1.1 The MBE machine

MBE is a deposition technique carried out in ultra-high vacuum, typically with background pressures of 10^{-10} Torr to avoid incorporation of impurities from the ambient. Atomic or molecular beams of different elements impinge on a heated substrate, and may form thin crystalline films, wires and particles [35]. Generally, the growth rates are low, typically 1 µm/h ($\sim$1 ML/s for relevant materials) or less, to ensure sufficient migration of the impinging atoms on the growing sample surface. MBE is suitable for growth of complex multilayer structures, incorporating thin layers of different compositions with abrupt interfaces. Compared to other deposition techniques, as e.g. metalorganic chemical vapour deposition (MOCVD), MBE can be carried out with lower substrate temperatures during growth, preventing interdiffusion between layers composed of different materials. Layers with metastable compositions can then be formed [36].
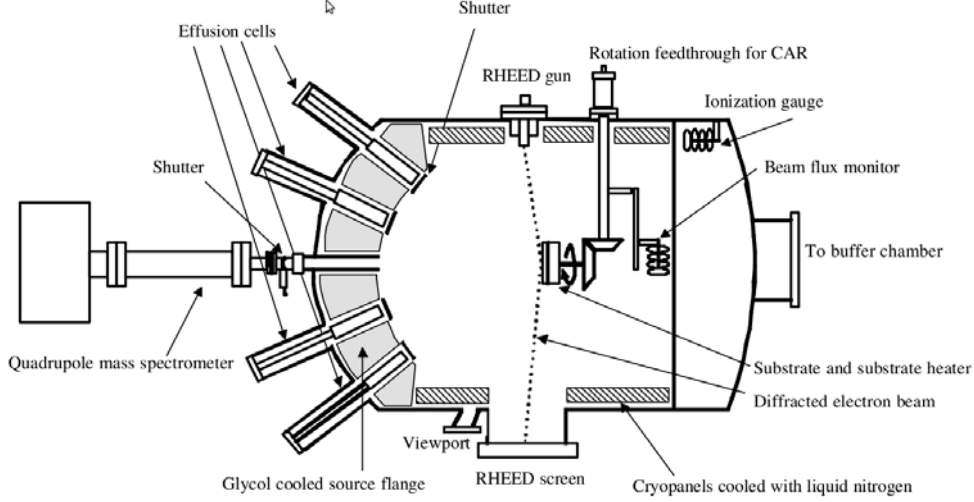
Figure 4.1: Schematic drawing of the MBE growth chamber used in this work. Only four effusion cells and one viewport (used for pyrometer measurements) are included in the drawing. The ion pump is also omitted. Taken from [36].

The MBE depositions in this thesis are performed using a Veeco Gen II Modular MBE system, shown schematically in Figure 4.1. The eight effusion cells are situated on one side of the growth chamber, and contains In, Ga, Al, As, Sb, Si, GaTe and Be. The last three are doping materials. The cells are positioned in a section of a sphere pointing towards the substrate in the sphere center. The substrate is placed on a substrate heater, which can be rotated to achieve uniform deposition across the sample. The substrate temperature is measured using a pyrometer through a viewport. The pyrometer gives correct temperatures above 580°C. For lower temperatures, the temperature is calibrated with the temperature for the transition (observed by RHEED) from the c(4x4) to the (2x4) reconstruction on GaAs as a reference point. The oxide desorption temperature at 580°C is also used to calibrate the pyrometer.

All effusion cells are equipped with mechanical shutters to turn on and off and the material beams in a controlled manner. The As cell is a valved cracker furnace. Evaporated As_4 atoms are channeled into a separate heater zone where they undergo multiple collisions at a very high temperature. In the growths in this thesis work $T_{As,cracker} = 900°C$, and As_4 dissociates to As_2 [35]. The valve allows rapid As flux changes, as need during QD growth since the As_2 flux used during growth of the (Al)GaAs barriers are much

higher than used during InAs QD growth. The In cell is a SUMO cell to achieve a stable and uniform flux across the substrate. A more detailed description of the MBE machine is given in [36].

4.1.2 Growth processes

The main processes on the growing surface during epitaxial growth are illustrated in Figure 4.2 [35]: (a) a beam of atoms or molecules are impinging on the surface and the adsorbed ad-atoms may then undergo (b) surface diffusion, (c) dimer formation, (d) attachment to existing islands, (e) island/step detachment, (f) island edge/step diffusion, (g) interdiffusion between monolayers. In addition, they can hop down (or up) from the top (bottom) of the island (h).
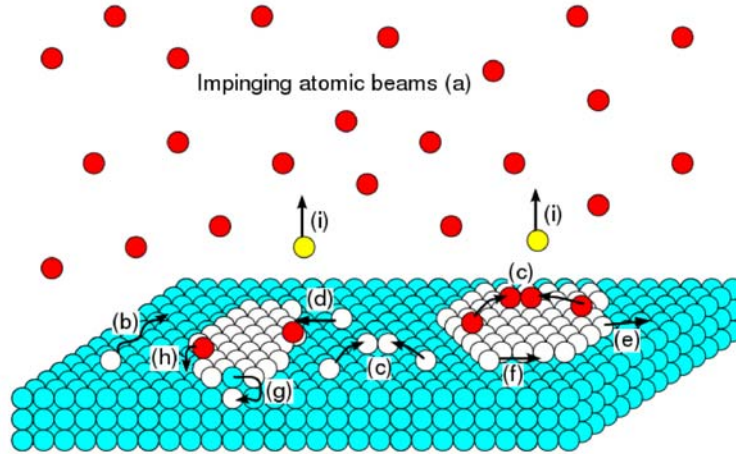
Figure 4.2: Schematic illustration of surface growth processes during thin film growth.

The sticking coefficient describes how large percentage of the imping atoms that are incorporated in the growing material. The sticking coefficient is approximately 1 for well adjusted growth parameters, but strongly varies with growth temperature and material fluxes. The growth rate is related to the evaporation rate from the material sources, and can therefore be controlled by the cell temperature if the sticking coefficient is known. In our experiments we have grown only III-V materials, normally with an excess of group V molecules. Then the group III beam flux alone determines the growth rate.

In epitaxial growth, a crystal film can be grown on a crystalline substrate if the two crystal structures are similar. The atoms in a crystal are arranged in a periodic lattice with the lattice constant a. If the film deposited on top of the substrate is of the same material as the substrate material (homoepitaxial growth), the atoms will adopt the structure of the underlying layers, forming a single crystal with the same unit cell in the substrate and in the growing film. If the incoming atoms are of a material with a smaller lattice constant than the substrate material, the growing film will be tensilely strained as the in-plane lattice constant will be the same as the substrate lattice constant, but smaller in the growth direction, see Figure 4.3a). If the incoming atoms are of a material with a larger lattice constant, a compressively strained film will be grown, where the lattice constant in the growth direction is larger than in the substrate surface plane, see Figure 4.3b). The growing film will relax and for defects if the film thickness exceeds a material dependent critical thickness [35].

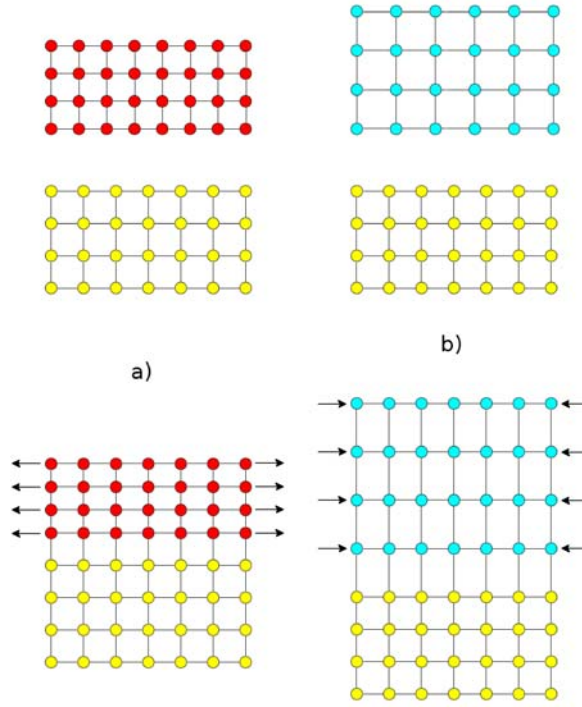

Figure 4.3: Epitaxial growth of strained layers on top of a substrate with lattice constant $a_{substrate}$. a) $a < a_{substrate}$ results in a tensilely strained film. b) $a > a_{substrate}$ results in a compressively strained film.

Epitaxial growth is divided into three growth modes [35], as illustrated in Figure 4.4. In the Frank-van der Merwe (FM)/layer-by-layer mode, the incoming atoms are more strongly bound to the substrate than to each other, i.e. $\gamma_{substrate} \geq \gamma_{interface} + \gamma_{film}$, where $\gamma_{substrate}$ is the substrate surface energy, γ_{film} is the film surface energy and $\gamma_{interface}$ is the interface energy between the substrate and the growing film. In Volmer-Weber (VW)/island mode, $\gamma_{substrate} < \gamma_{interface} + \gamma_{film}$, i.e. the incoming atoms are more strongly bound to each other than to the substrate, and islands are formed on the surface instead of a continuous film. The Stranski-Krastanov (SK) growth mode is a combination of the two modes described above. During growth of the first monolayer(s), $\gamma_{substrate} \geq \gamma_{interface} + \gamma_{film}$ and the film grows layer-by-layer. After the film thickness reaches a material dependent critical thickness (Θ_c), the atoms become more strongly bound to each other than to the substrate, $\gamma_{substrate} < \gamma_{interface} + \gamma_{film}$, and island formation is favored. The SK mode is related to the strain in the growing film due to difference lattice constants of the substrate material and the epilayer, as explained above. Whether the growth mode is FM, SK or VW depends on the lattice mismatch between the epilayer and the substrate (ϵ), and the amount of deposited material of the epilayer (θ), as illustrated in Figure 4.5.

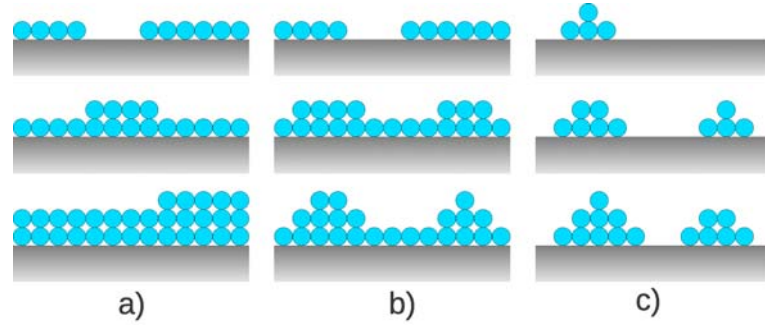**Figure 4.4:** Schematic illustration of the three epitaxial growth modes. a) Frank-van der Merwe mode, b) Stranski-Krastanov mode and c) Volmer-Weber mode.

In this thesis, self assembled QDs are grown utilizing the SK growth mode for the InAs/(Al)GaAs(001) system. As self assembled quantum dots are spontaneously formed without the need of lithography, they have received a lot of attention during the last three decades.
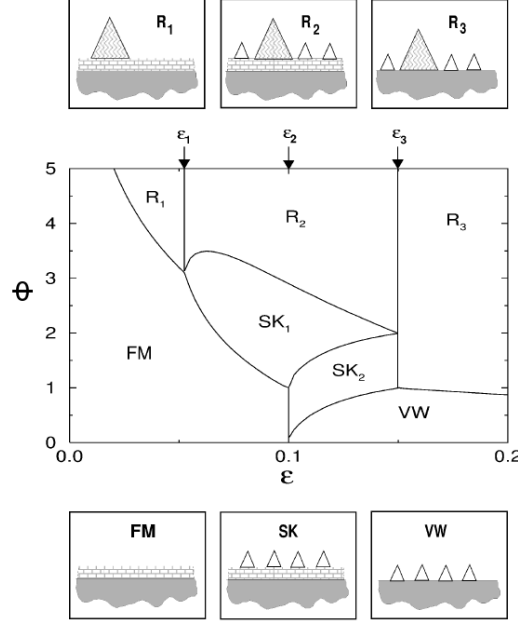
Figure 4.5: Growth mode as a function of lattice mismatch (ϵ) and monolayer coverage of the epilayer (θ). In the R growth modes, ripened QDs co-exist with the coherent QDs. Taken from [37] (slightly modified).

4.1.3 Stranski-Krastanov grown InAs/(Al)GaAs quantum dots

Stranski-Krastanov (SK) growth is caused by lattice mismatch between the substrate and the growing film [38]. For InAs growth on GaAs and AlGaAs the lattice mismatch is approximately 7%. For the parameters used to calculate the diagram in Figure 4.5, SK growth will occur when the coverage is larger than around 1.7 ML. For lower coverages, the growth mode is FM. The initial understanding of the growth process was that the strain energy in the growing InAs film increases due to the accommodation of mismatch strain between the InAs epilayer and the GaAs substrate. Eventually, the InAs film relaxes and 3D islands are formed. The strain is relieved by formation of misfit dislocations in the islands. However, several studies published the last decade indicate that the growth mode is more complex than first assumed. First of all, QDs with size smaller than a certain limit are coherent, i.e. dislocation free. For appropriate growth conditions, the formation of defect-containing QDs is completely suppressed. Secondly, several studies report a larger total QD volume than the deposited amount of InAs [39–41],

Ga incorporation into the QDs [39, 40] and a varying critical thickness prior to the 2D-3D transition [42, 43], indicating In-Ga intermixing during wetting layer formation and wetting layer or substrate erosion [44]. Both the QD volume, Ga incorporation and the critical thickness varies with growth parameters during InAs deposition, as substrate temperature, As flux, InAs growth rate and the amount of deposited InAs, i.e. the intermixing and/or substrate erosion varies with growth parameters. This topic is further discussed in Papers II-V.

The influence of the growth parameters on the QD formation process, the QD density, the QD sizes and the optical quality is thoroughly studied in Papers I-V. The main focus of the growth of the QD samples was to achieve high QD density ($> 10^{11}$ cm^{-2}), a narrow size distribution, and a high optical quality. The influence of the growth parameters on the growth of InAs/GaAs QDs are reported in numerous papers. The most important work on the influence of the substrate temperature are found in Refs. [45–56], the InAs coverage in Refs. [45, 51, 52, 54, 57–69], the InAs growth rate in Refs. [45, 47, 54, 59, 70–72] and As flux in Refs. [45, 47, 53, 55, 58, 64, 73].

The samples are characterized by several techniques. Reflective high energy electron diffraction (RHEED) is used in-situ during growth, while scanning electron microscopy (SEM), atomic force microscopy (AFM) and photoluminescence (PL) were done ex-situ.

Most of the samples studied in this work consist only of an (Al)GaAs buffer and two QD layers separated by a (Al)GaAs spacer, see Figure 4.6. The uncapped (but oxidized) surface QDs are studied by SEM and AFM. The structure of buried QDs in a few samples are studied by transmission electron microscopy (TEM).
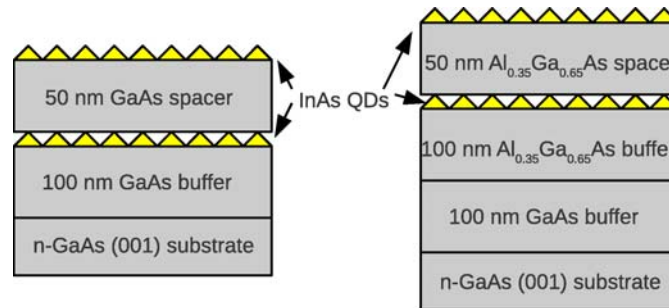

Figure 4.6: Schematic structures of the QD samples studied in this thesis.

4.2   Characterization

4.2.1   RHEED

Reflective high-energy electron diffraction (RHEED) is an in-situ characterization technique used to monitor the structure of sample surfaces during growth [35,74]. A beam of high energy electrons, typically 3-15 eV, directed towards the sample at grazing incidence, typically 1-2 degrees, penetrate only the outermost atomic layers of the sample surface and is diffracted on to a fluorescent screen positioned at the opposite side of the growth chamber, see Figure 4.1. The pattern on the fluorescent screen is a diffraction pattern of the penetrated layers. By monitoring the diffraction pattern during growth, the evolution of the substrate surface can be detected/observed.
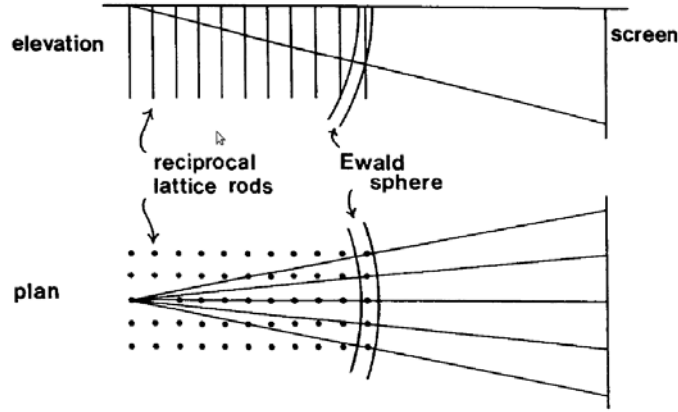

Figure 4.7: The crystal lattice in reciprocal space. In reciprocal space, the third dimension is not defined, but represented as lattice rods normal to the sample surface. Reciprocal lattice points incident with the Edwald sphere result in constructive interference and form bright, intense spots on the fluorescent screen. Taken from [74].

As the electrons enter the sample at a low angle, the electrons essentially interact with a 2D sample. In real space the third dimension is missing. In reciprocal space the third dimension is not defined and is therefore represented by rods normal to the real surface, see Figure 4.7. $k_0 = \frac{2\pi}{\lambda}$ is the reciprocal lattice vector. k_0 is positioned at the reciprocal lattice point designated as the origin of the reciprocal lattice space, and its length is the radius of the Edwald sphere. Constructive diffraction occurs when a reciprocal lattice points intersects with the Edwald sphere. The Edwald sphere

has a finite width due to a small spread in the electron beam angle, thermal vibrations of surface atoms and the fact that the surface of the substrate or sample never is completely flat. The intersections therefore appear as elongated streaks on the phosphorous screen. If the surface is rough, or contain 3D features as QDs, the scattered beam will leave the scatterer from a different spot than where it entered as the electrons interact with a 3D sample. The diffraction pattern is therefore spotty and not streaky, as described above.

RHEED can be used in static or dynamic mode. The dynamic mode can be used for growth rate calibration of the incoming material fluxes. In ideal Frank-van der Merwe growth, the incoming adatoms form one full monolayer before growth of the next layer start, as illustrated in Figure 4.8. The RHEED spots will be intense for flat layers and weak for half filled layers, due to the roughness of the film, as explained above. The spot intensity therefore oscillates as the film grows. Maximum intensity is achieved for full layers and minimum intensity for half layers. The growth rates of group III materials can be calibrated by measuring periodicity of the oscillating intensity for growth in an 'As atmosphere'.
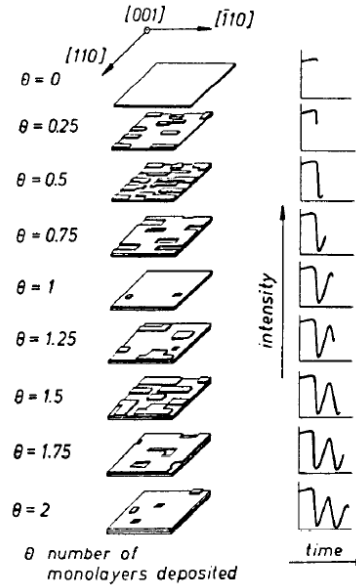

Figure 4.8: Calibration of material growth rate using RHEED in dynamic mode. Taken from [74].

The static RHEED mode is used for studying surface reconstructions

during growth. In many materials the surface reconstructions change at specific temperatures, and can be used as temperature calibration of e.g. pyrometers used for controlling the growth temperature. In our experiments, at GaAs substrates, we have used the reconstruction transition from c(4x4) to (2x4), which occurs around 515ºC, to calibrate the growth temperature.

4.2.2 Scanning electron microscopy

In scanning electron microscopy, electrons are used to image the sample instead of light, as in an optical microscope [75, 76]. The electron wavelength is much smaller than the wavelength of light, and a higher resolution is achieved. When electrons impinge a sample surface they will penetrate the sample for a certain distance before they encounter and interact with a sample atom. The region limited by the penetration depth is called the interaction volume, as illustrated in Figure 4.9a). When the impinging electrons interact with the atoms in the sample, some electrons are backscattered with the same energy as the incoming energy due to elastic scattering. All electrons with energy > 50 eV are defined as back scattered electrons (BSE). Other electrons are inelastically scattered due interactions between the electrons and the sample. Ionization of the sample atoms leads to generation of secondary electrons (SE), with energy smaller than 50 eV. In addition, some Auger electrons are produced and characteristic X-rays are generated, as illustrated in Figure 4.9b).

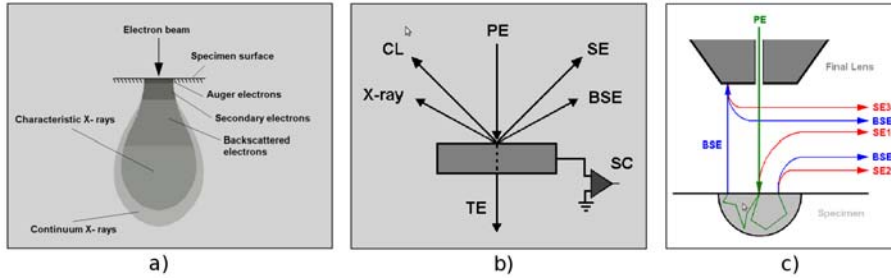**Figure 4.9:** Illustrations of a) the interaction volume, b) the products of the interaction between the primary electron (PE) beam and the sample atoms and c) the different types of secondary electrons (SE) formed during the interaction. Taken from [75]. In addition to SE and BSE, X-rays are generated and in some cases also visible light due to cathodoluminescence (CL). A portion of the electrons transmit through the material (TE).

In this study we used a Zeiss Supra 55 and a Zeiss Ultra 55 microscope to image the QD samples. The main setups of these machines are shown in Figure 4.10a). The electrons in the electron beam is produced in a thermal field emission tip and accelerated to the user set voltage on their way to the anode. This setup includes a beam booster, situated directly behind the anode, which is held at a potential of 8 kV. The beam booster ensures that the energy of the electrons in the entire beam path is always 8 kV higher than the user set acceleration voltage. This is to reduce the effect of magnetic stray fields that might influence the beam path. The electrostatic lens creates an opposing field and reduces the electron voltage down to the user set voltage. The field lens is used to collimate the beam into a relatively parallel beam. The aperture limits the beam width. Varying the aperture influences the beam shape and the beam edge sharpness. A small aperture typically has a larger depth of field than a large aperture, i.e. features with a larger height variations are in focus for a small aperture. Before entering the sample surface, the beam is focused into a probe point by the magnetic lens. Lens defects and contamination on e.g. the aperture can cause variations in the electron beam cross section. Generally, an elliptic cross section is formed instead of a circular one. Then, a circular object would look oval in the resulting SEM image. This effect is called astigmatism and is corrected by a series of coils surrounding the electron beam called a stigmator. The distance between the column and the sample surface is called the working distance (WD). A higher lateral resolution is achieved when reducing the WD. However, the depth of field is decreased as the sample is scanned with a wide cone of electrons.

The SE and BSE modes are most commonly used in SEM imaging. The SEM images in this thesis are formed using SE. The secondary electrons are generated in the upper part of the interaction volume and contain information about the sample surface, as illustrated in Figure 4.9a). The SE are products of inelastic scattering of the primary electrons (beam electrons) by the atomic core or by the electrons of the sample atoms. They are subdivided into different groups, as illustrated in Figure 4.9c): SE1 are both generated in and leave the surface from the spot center, SE2 are generated by multiple scattering processes and leave the surface from a different position than the spot center and SE3 are generated by BSE far away from the spot center and are not important for image formation. SE1 and SE2 are collected as these are generated in or close to the spot center.

The SE-detector is typically positioned next to the electron gun, see Figure 4.10b). However, when scanning at low working distances, the SE's can be blocked on the way to the detector. Then, the In-lens detector is a
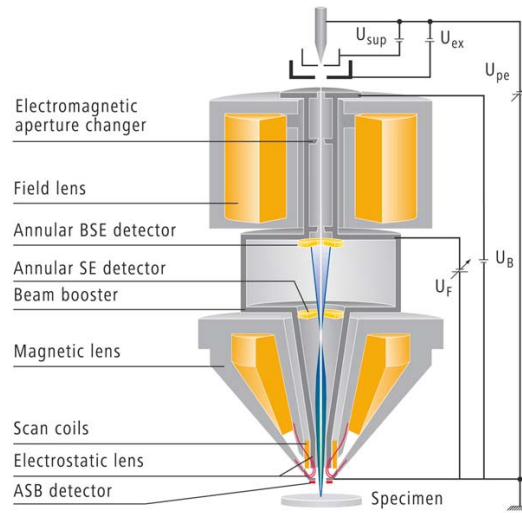
(a)
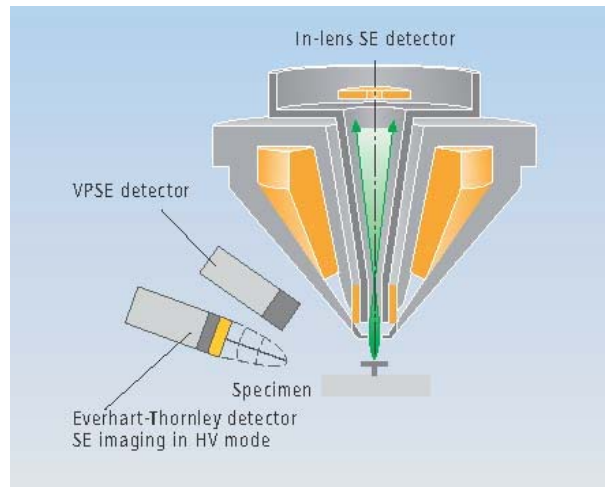
(b)

Figure 4.10: a) Illustration of the SEM instruments. b) The in-lens detector is positioned in the beam path. Taken from [75].

better choice as it is situated above the objective lens and detects directly in the beam path.

In this study, we have imaged nanometer scaled QDs. To increase the lateral resolution, a low acceleration voltage was chosen in combination with a small WD (1-3 mm) to reduce the penetration length of the primary electrons. Then the SE mainly escape from sites close to the surface. The aperture opening was reduced compared to the standard opening to increase the depth of field.

4.2.3 Transmission electron microscopy

In transmission electron microscopy (TEM), high energy electrons are transmitted through the sample and focused on a fluorescent screen. The electrons impinging the sample are accelerated to a higher voltage, typically 80-300 keV, compared to the electron beam voltage used under in SEM characterization [77]. The sample thickness must be small (<1000 nm) as the electrons must be able to pass through the sample. The electrons carry information of the interior of the sample as they have been involved in several scattering processes within the material. After interacting with the sample atoms, the electrons are either directly transmitted, elastically or inelastically scattered or result in bremsstrahlung X-rays, dependent on the scattering processes. A bright field (BF) image is formed if only electrons being directly transmitted are used. If the beam of directly transmitted electrons are excluded and only the diffracted electrons are used, a dark field (DF) image is formed.

As in any imaging technique, contrast is important for a achieving a high image quality. An electron interacting with an atom with a high Z will be more strongly scattered than if it was to interact with an atom with a low Z. Elements with high Z therefore appear darker than elements with low Z in a bright field (BF) image if the sample thickness is the same for both elements. The contrast will change by varying the crystal structure and orientation of the crystal with respect to the electron beam. Strained areas in the sample will appear at a lower or higher contrast compared to unstrained areas. The intensity of the image is a sum of the contribution from the Z contrast and the strain contrast.

A focused beam scans the sample in a raster pattern during scanning transmission electron microscopy (STEM). The electrons transmitted through the sample are collected. If electrons scattered into higher angles are collected a high angular bright field HAADF-STEM image is formed. In this mode, the intensity is approximately increasing with Z as $I \approx Z^2$ and the heavy atomic species can easily be detected. The strain is best visualized collecting electrons in lower angles in a low angular bright field LAADF-STEM image.

4.2.4   Atomic force microscopy

Atomic force microscopy (AFM) is a technique which images the topography of a sample surface using a sharp tip which interacts directly with the surface [78,79]. A high-resolution three-dimensional image is produced probing the repulsive and attractive forces existing between the probe (stylus) and the sample surface.

The sharp tip is placed on the apex of a cantilever, see Figure 4.11. The sample is placed on a piezoelectric scanner which can move the sample in x-, y- and z-direction with a sub-nanometer precision when a high voltage is applied. The tip is positioned close to, or in contact with, the sample during the scanning. The cantilever deflects due to surface topography or variation in forces between the tip and the surface as the cantilever moves across the surface. A laser beam is incident on the cantilever's upper surface and reflected onto a position sensitive photodetector.
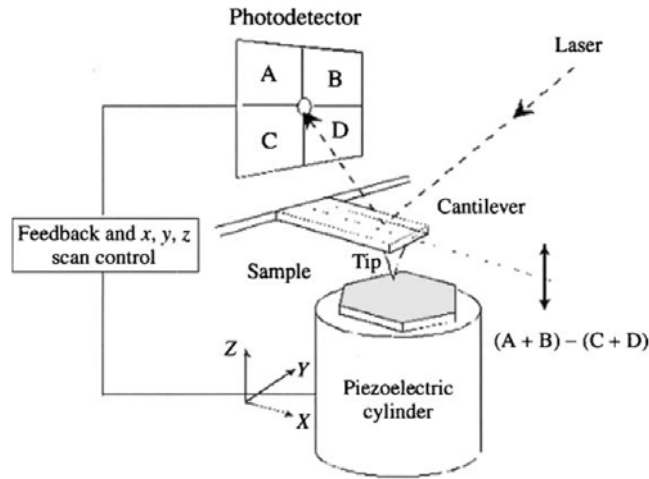
Figure 4.11: Schematic illustration of an AFM setup. Taken from [79].

There are two main modes of AFM imaging: Contact mode and tapping mode. In contact mode, the tip is in contact with the sample surface and a repulsive force is always present due to the overlapping electron orbitals of the tip atoms and the sample atoms. Contact mode can be performed with constant force or variable force. In constant force mode, the deflection, and thus also the force, of the cantilever is constant. If the cantilever deflection is changed due to the surface topography, the z-height is altered so the cantilever deflection remains constant. In this mode the z-position

is monitored as a function of the x- and y-position. During variable force imaging, the z-height remains constant and the deflection is monitored to produce the topographic image. Variable force can with benefit be used for smooth surfaces where the surface features are low. For these kind of surfaces, the resolution can be improved compared to the constant force mode. In both modes the height tracking precision and lateral resolution is high. The lateral resolution is down to atomic resolution for appropriate imaging conditions. The draw-back is that the tip applies a high local pressure and shear stresses on the surface, which can be altered. Also, material from the sample surface might stick to the tip and alter the image.

In tapping mode, the cantilever is put into oscillation by an electrical oscillator and vibrates at a value close to its resonant frequency. As the cantilever sample moves across the surface, the oscillation amplitude will vary as the tip touches areas with different topography. The amplitude variations are detected by the photodetector and the feedback system. Tapping mode will generally not alter the sample surface.

The AFM studies performed in this thesis is mainly performed in contact mode using constant force.

4.3 Photoluminescence spectroscopy

As the QDs are to be used in a solar cell, optimizing the optical quality is crucial, i.e. minimizing the non-radiative Shockley Read Hall recombination. A common characterization technique used for analysis of the optical quality of semiconductor materials is photoluminescence spectroscopy (PL). In this technique, samples with a lot of non-radiative recombination is easily detected when compared to samples with low non-radiative recombination.

PL is a nondestructive method used to investigate the electronic structure of semiconductors [35]. A light source illuminates the sample. If the photon energy (E_{ph}) is larger than the semiconductor bandgap, the light is absorbed and an electron-hole pair is formed. The charge carriers will thermalize, as explained in Section 2.2. An electron in the CB recombines radiatively with a hole in the VB and emits a photon. The process is illustrated in Figure 4.12. The energy levels of holes and electrons in QDs are lower than the VB and CB edge, respectively. Charge carriers in the VB and the CB can therefore relax into the QD if they do not recombine on the way. Again, the electron in the CB of the QD can radiatively recombine with a hole in the QD VB, by emitting a photon. The emitted photons are dispersed by a monochromator and collected in a detector. The resulting PL spectrum from the material will contain both PL peaks from the

bulk material and from the QDs. In this work, the PL spectroscopy was performed at 2 K to suppress thermal escape of the carrier out of the QDs.
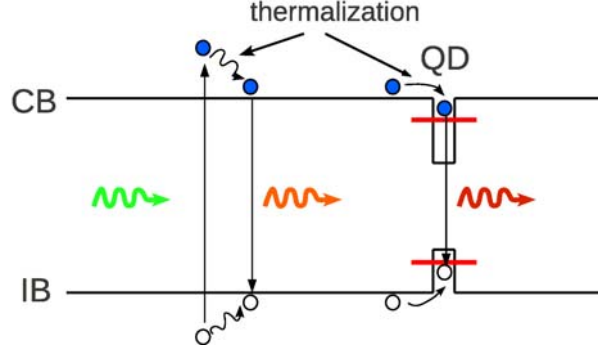

Figure 4.12: Schematic illustration of photo-excitation and radiative recombination. The process to the left illustrates absorption of a high energy photon, exciting a electron high up in the CB and similar for the hole in the VB. The carriers are relaxed. If they recombine radiatively, they emit a photon with energy equal to the bandgap. The process to the right illustrates an electron-hole pair which relaxes further down into the confined states of the QDs. In this case, the energy of the emitted photon equals the energy difference between the initial state and the final state.

4.4 Solar cell fabrication and testing

The QD-IBSCs made in this ph.d. project were characterized by external quantum efficiency (EQE) and current-voltage (IV) measurements. EQE and IV characterization has not been performed by me, but a description is included for completeness.

4.4.1 Solar cell design

As studying the influence of the growth parameters became the main topic of my thesis, no in-depth study of the design of solar cells has been performed. Initially, we therefore used the cell design reported by Blokhin et al. [21] as a guideline.

The solar cell designs of the samples presented in Papers VII-IX are shown in Figure 4.13. The cells were grown to study the influence of growth temperature, As_2 flux, numbers of QD layers (5 or 20) and removal of the wetting layer on the solar cell performance.
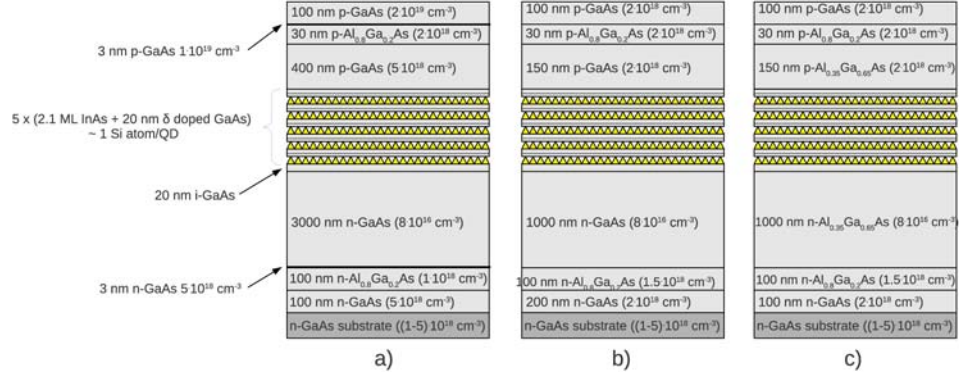
Figure 4.13: Basic structure of solar cells presented in Papers VII (a and b), VIII (a) and IX (b and c).

In paper IX, a series of QD-IBSCs were grown to study if the solar cell voltage increases when changing the bulk solar cell material from GaAs to $Al_{0.35}Ga_{0.65}As$. The $Al_{0.35}Ga_{0.65}As$ QD-IBSCs were compared to similar grown InAs/GaAs QD-IBSC.

4.4.2 Solar cell processing

The cells were processed at IB-LAB, Universidad Politécnica de Madrid. The front contact consist of AuGe:Ni:Au and the back contact of Au:Zn:Au. The processing is as follows: First the back electrode (225 nm of AuGe:Ni:Au) is deposited at room temperature and then annealed at 370ºC in a forming gas. Next, the circular front electrode is defined by lithography, and the front surface is wet etched ($1H_2SO_4$:$8H_2O_2$:$160H_2O$) to clean the surface prior to front electrode deposition (270 nm of Au:Zn:Au). The front electrode processing is finalized by a lift-off process and an anneal at 330ºC in a forming gas. Finally the circular cells (ca 1 mm in diameter) are isolated by a mesa wet etch ($3H_3PO_4$:$4H_2O_2$:$1H_2O$).

4.4.3 Solar cell testing

The solar cell characterization was performed at IB-LAB, Universidad Politécnica de Madrid.

Current-voltage characteristics

The current-voltage characteristics (IV) of a solar cell is obtained by applying a bias voltage to the solar cell and measuring the current while the cell is illuminated by a spectrum similar to the solar irradiation. In this thesis, the AM1.5D low Aerosol spectrum at power 90 mW/cm^2 was used.

Quantum efficiency

The quantum efficiency (QE) indicates the amount of current produced by the solar cell for a given wavelength [80]. An integration of the QE over all wavelengths result in the total current generated for a given spectrum. For the external QE (EQE), the reduction in current due to surface reflection (R) in is included, while R is taken as 1 for the internal QE (IQE).

Chapter 5

Status of QD-IBSC research

Since Luque et al. in 2000 proposed using sheets of closely spaced QDs to form the intermediate band [81], several groups worldwide has joined the quest for the realization of a QD-based IBSC (QD-IBSC). So far, the success is somewhat modest. Many of the reported QD-IBSCs *do* show increased current density, but the QD implementation is, in most cases, accompanied by a reduced open circuit voltage. The net effect has in most cases been a lowering of the conversion efficiency, compared to a reference cell without QDs.

In this chapter I summarize the most important milestones during a decade of research and the remain challenges for the QD-IBSC. Most of the studies has been concentrating on the InAs/GaAs material system, but Ge/Si QD-IBSCs have also been reported.

5.1   The first attempts

Six years after the first proposal, and after several theoretical reports, Luque et al. [82] and Norman et al. [83] published the first experimental papers of In(Ga)As/GaAs QD-IBSCs, where they showed evidence for sub-bandgap absorption and three separate quasi-Fermi levels. In 2006, Marti et al. proved that both transitions, from VB to IB and from IB to CB, are optically active at low temperatures [84]. However, their studies show that the transition from IB to CB is weak [85] and only detectable at low temperatures. In 2007 the same group showed that the internal QE and the carrier lifetime in the p-emitter, grown on top of the QD stack, is reduced with increasing number of QD layers due to relaxation and formation of stacking faults [86]. In 2008 the first study focusing on strain balancing using $GaAs_{1-x}P_x$ as a spacer between the InGaAs QD layers was published [22].

Later, several papers on strain balancing have been publised, e.g. Hubbard et al. studied the effect of a GaP layer between the QD layers [24], Antolin et al. studied the effect of InAlGaAs layers on top of the QDs and varying and barrier thickness in [87], and Takata et al. and Oshima et al. studied the influence of introducing nitrogen into the barrier material [23,33]. Even though TEM characterization indicate good structural quality and PL measurements show increasing emission with the number of QD layers, none of the reported cells have showed increased efficiency compared to the corresponding 'QD-free' reference cells. In 2009 by Blokhin et al., reported an InAs/(Al)GaAs QD-IBSC with an efficiency of 18 % compared to 23 % in the reference cell without strain balancing layers [21]. In 2010 Guimard et al. showed how the growth parameters used during QD growth affect the solar cell performance, especially V_{oc} [25]. They also compared QD-IBSCs with solar cells containing only the wetting layers (WL-IBSC) (InAs deposition stopped before the 2D-3D transition). When grown with appropriate conditions, V_{oc} was similar in WL-IBSCs and QD-IBSCs, indicating that the WL and the QDs share quasi-Fermi level in the CB. Guimard et al. also reported the best cell, when comparing to the corresponding reference cell, so far. Their QD-IBSC had an efficiency of 13.1 % compared to 13.7 % in the reference cell. In 2011 Bailey et al. reported strain balanced InAs/GaAsP QD-IBSCs with $V_{oc} \sim 1$V, only 5 % lower than the GaAs reference cell. Their cells also showed slightly increased I_{sc} compared to the reference. In 2012 the same group reported increased V_{oc} when reducing the InAs coverage (1.8 ML) to avoid formation of large, defect-containing QDs [88].

Several studies are reported, but the above describes the main time line for the improvements of experimental QD-IBSCs. Through these studies, the main challenges of the QD-IBSC are made visible. We will discuss these in the following section.

5.2 Challenges for QD-IBSCs

5.2.1 Reduced V_{oc}

So far, all attempts in making an InAs/GaAs QD-IBSC with or without strain compensating layers has resulted in reduced V_{oc}. The main reason for this is most likely defect formation during stacking.

In addition, one should note that the comparison between an InAs/GaAs QD-IBSC and a GaAs SC is not fair. Even though the VB offset is non-zero, the high effective mass of the holes result in a number of closely spaced

confined levels forming a quasi-continuum with the VB, see Figure 5.1. The
Fermi level of the VB is thus determined by the Fermi level of the holes in
the QDs. The presence of the wetting layer introduces at least one energy
level below the CB edge. This level is not separated from the CB by a zero
density of states. The electrons in the CB are therefore able to relax down to
the WL energy level. The resulting effective bandgap of the GaAs barriers is
therefore more likely to be in the order of 1.3 eV than 1.42 eV [17]. However,
almost all reported QD-IBSCs report a larger reduction in V_{oc} than what
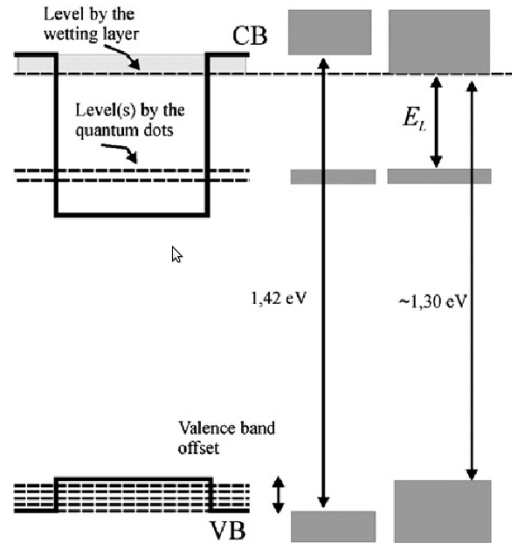can be accounted for by VB offset and the presence of WL.

Figure 5.1: Simplified band structure of a InAs QD in a GaAs spacer indicating
the reduced effective band gap of the host material due to valence band offset and
the presence of the WL. Taken from [17]

5.2.2 Improvement in I_{sc}

Many studies of QD-IBSCs report improved current densities when com-
paring to their reference cells. However, the increase is not large enough to
improve the efficiency. To achieve a coupling of the electron wave functions
and achieve a high absorption, the QD density should be as high as possible.
Marti et al. suggest an interdot distance of 10 nm [89], implying a sheet
QD density of 10^{12} cm^{-2}. QD densities used typically are 10 to 100 times
less. So far, the limited sheet density has been compensated by increasing

the number of QD layers. As the number of QD layers increases, accumulated strain is relieved through defect formation which forms non-radiative recombination centers trapping the charge carriers and reducing both I_{sc} and V_{oc}.

For I_{sc} to increase it is crucial that all three transitions (VB-IB, IB-CB and VB-CB) are active. An effective bandgap $E_g \approx 1.3$ eV, as described above, result in $E_L < 0.2$ eV. The IB is then probably thermally coupled to CB. This IB-CB transition will then only be optically active at low temperatures, as found by Antolin et al. [85].

When the QDs are placed inside the pn junction, they are placed inside an electric field, see Figure 5.2. This implies that the QD energy level forming the IB is above the Fermi level for the QDs close to the p side and below for the QDs close to the n side. The energy levels of the former QDs will be empty and the transition between IB and CB will not function. The energy levels of the latter QDs will be filled and the transition between the VB and IB will not be efficient. To achieve efficient transitions, the QD layers should be placed in near flat-band-region. This was tested in Ref. [90] by a modified pn junction to achieve flat bands inside the pn junction. However, when the bands are flat, the charge separation is not efficient, resulting in increased recombination.
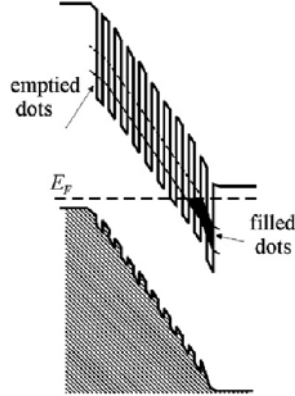

Figure 5.2: Simplified band diagram of QDs implemented in the solar cell pn junction. Taken from [89]

5.3 Proposed solutions and status

Several theoretical works has presented candidates for new material systems. Franceschetti et al. [91] propose to use a spacer material between the QD layers with a larger bandgap than the bulk solar cell material to decrease the rate of recombination in the IB region, Dahal et al. [92] reported studies of different compositions of InAs, InP, $InP_{1-x}Sb_x$, $InAs_{1-x}P_x$ and $InAs_{1-x}Sb_x$ as QD materials in an $Al_{1-x}In_xAs$ or $Al_{1-x}Ga_xSb$ host material and Linares et al. [93] studied the impact of varying composition of $InAs/Al_xGa_{1-x}As$, $InAs_{1y}N_y/AlAs_xSb_{1x}$ and $InAs_{1z}N_z/Al_x[Ga_yIn_{1y}]_{1x}P$. To our knowledge, no experimental studies has been published yet on these material systems. By choosing another material system with bandgaps closer to the optimal bandgaps, the IB will be thermally and electrically separated from the CB and the IB-CB transition, which hopefully will increase the I_{sc}. However, one should keep in mind that as long as the QDs are grown in Stranski-Krastanov mode, with a wetting layer present below the QDs, and the valence band offset is non-zero, the voltage will be lower than a similar reference cell without the QDs due to the reduction in effective bandgap. This is not crucial because on can simply choose a material with slightly larger bandgap and allow for the bandgap reduction. The crucial point is to avoid a reduction in V_{oc} due to defect formation.

To increase I_{sc}, several layers with a high density of QDs must be grown as the QD volume within one layer is vanishingly small. Then the challenges of stacking must be overcome. As described above, several groups study how to compensate the strain during growth of a QD stack by introducing strain compensating layers of GaP [24, 90], InAlGaAs [87] or inclusion of P [22] or N [23, 33] into the GaAs barrier. These challenges will be of equal importance when changing to another material system if the QDs are to be formed by the strain induced Stranski-Krastanov mode.

5.4 Our contributions

The main focus of this thesis is to gain further insight in the fabrication of QD-IBSC materials by MBE. Based on the MBE growth optimization studies we have made several series of QD-IBSCs where various aspects of the QD growth and the impact on solar cell performance are studied.

So far, most other groups have focused on how to achieve a high QD volume density by stacking several QD layers. However, in light of the problems with defect formation during QD stacking, we found it fruitful to try to achieve a high QD density within each QD layer. In addition, a high

density will improve the coupling and the associated delocalization of the electronic states. In Paper VII, the QD density is varied in QD-IBSCs.

In an attempt to increase V_{oc}, we looked into removal of the WL. By capping the QDs with a thin AlAs layer we found that the WL was removed. When introducing AlAs capped InAs QDs into the QD-IBSC we found that the V_{oc} increased 0.2 eV, as described in Paper XI.

As described earlier, the InAs/GaAs material system is not optimal for QD-IBSCs due to the small bandgap of GaAs and the large effective bandgap in InAs/GaAs QDs resulting in too small E_L. We therefore replaced GaAs by $Al_{0.35}Ga_{0.65}As$, which has a bandgap of 1.86 eV. The InAs/$Al_{0.35}Ga_{0.65}As$ QD-IBSCs showed a strong increase in V_{oc} compared to similar grown InAs/GaAs QD-IBSCs, as described in Paper IX.